Supplementary Information

Facile Strategy to Synthesize Cesium Gold-based Bromide Perovskites: An Integrated Experimental and Theoretical Approach to Study Temperature-dependent Structural and Optical Properties

Bhawna,[a] Vikram,[a,b] Mrinmoy Roy,[a] Supriti Ghorui,[a] Aftab Alam[a] and M. Aslam[a*]

[a]Indian Institute of Technology Bombay, Mumbai, India

[b]Department of Chemistry, University of Reading, Whiteknights, Reading, RG6 6AD, UK

[*]Corresponding Author: m.aslam@iitb.ac.in

(A) Experimental section

(1) Chemicals

For the synthesis of various gold-based bromide perovskites, the following chemicals were used as received without any further purification: Cesium chloride (CsCl, Sigma-Aldrich, 99.9%), gold chloride ($AuCl_3$, Sigma-Aldrich, 99.9%), hydrobromic acid (HBr, 48% solution), and de-ionized (DI) water.

(2) Synthesis Procedure

$CsAuCl_4$ (x = 0 µl of HBr): For the preparation of $CsAuCl_4$, first the individual solution of stoichiometric CsCl and $AuCl_3$ are made in DI water and are kept at low temperatures (~5-10°C). After mixing for half an hour, the CsCl aq. solution is poured into the solution of $AuCl_3$ solution immediately, resulting in a yellow precipitate.

$CsAuCl_4$ with x = 25, 50, 75, 100, 200, 300 and 500 µl of HBr: To the diluted solution of this yellow precipitate, HBr in the amount of 25, 50, 75, 100, 200, 300 and 500 µl are added. The final mixture is kept on stirring for half an hour. The resultant precipitate is then separated out from the supernatant using centrifugation (8000 rpm for 10 mins) and is washed with cold DI water. The process is repeated twice, and the precipitate is then dried in a desiccator for several days.

(B) Computational Details:

To perform the Density Functional Theory (DFT)[1] based ab-initio calculations, Vienna Ab initio Simulation Package (VASP)[2-4] was used with plane-wave basis set and Projector Augmented Wave (PAW)[5] pseudopotentials with PBE exchange-correlation functional.[6] A

plane wave energy cut-off value of 500 eV was used. The tetrahedron method with Blöchl corrections[7] was used for better accuracy in the electronic structure properties. The conjugate gradient algorithm was used to optimize the cell volume, shape, and atomic positions for all the structures with a force convergence tolerance of 0.01 eV/Å on each atom. A tolerance of 10^{-6} eV was used for the convergence of self-consistent-field (scf) calculations. The Brillouin zone sampling was done using automated Γ (gamma) centred K point mesh. A fully converged K-point mesh of 20×20×20 for cubic phase, 14×14×10 for monoclinic phase and 18×18×12 for tetragonal phase was used for the scf calculations.

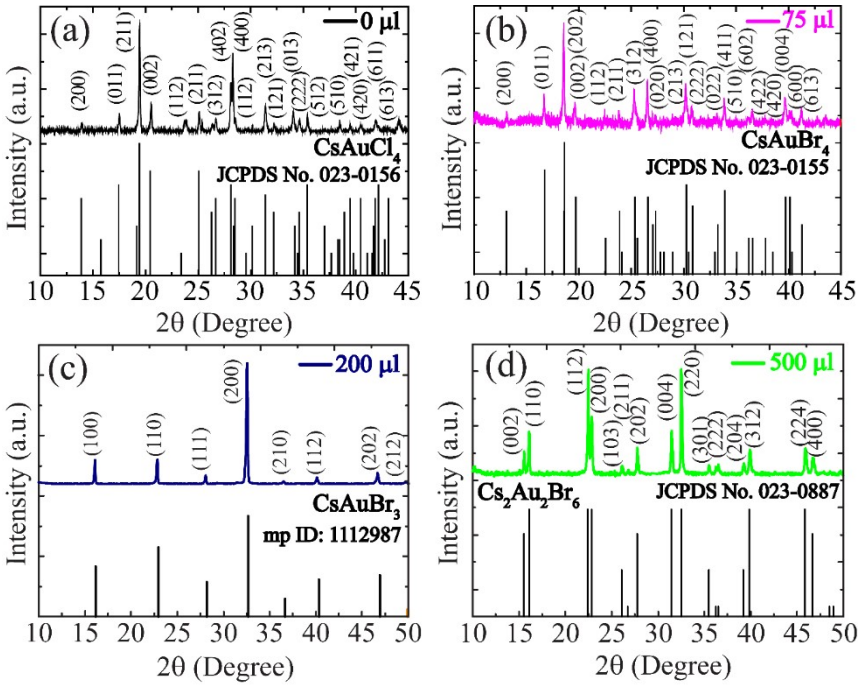

Figure S1: XRD data of $CsAuCl_4$ compounds with x = 0, 75, 200 and 500 µl HBr matches with the JCPDS data of (a) monoclinic $CsAuCl_4$ (black), (b) monoclinic $CsAuBr_4$ (pink; JCPDS card no: 023-0155), (c) cubic $CsAuBr_3$ (violet; materials project ID: mp-1112987) and (d) tetragonal $Cs_2Au_2Br_6$ (green; JCPDS card no: 023-0887), respectively.

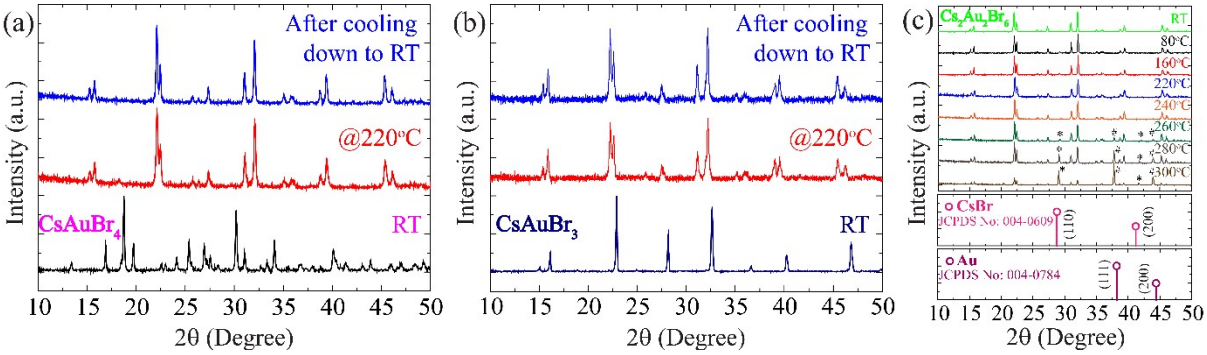

Figure S2: XRD profiles for (a) $CsAuBr_4$ and (b) $CsAuBr_3$ after heating the samples to 220 °C and then cooling them down to RT to test the reversibility of the phases. Stability test for

$Cs_2Au_2Br_6$ under temperatures ranging from RT to 300 °C. Side phases corresponding to the plane (110) and (200) of CsBr (JCPDS No.: 004-0609) and (111) and (200) of Au (JCPDS No.: 004-0784) arise for temperatures above 240 °C. This degradation is mainly due to the decomposition of gold bromide to metallic gold at temperatures above 250 °C.

The crystal structure of $CsAuBr_4$ has isolated Cs^+ cations lying in between the layers of square planar $[AuBr_4]^-$ anions (Figure S7(a)). This isolation of Cs^+ cations over $[AuBr_4]^-$ sites can be attributed to the rod-like morphology obtained for $CsAuBr_4$ as studied using Scanning Electron Microscopy (SEM).[8] The $CsAuBr_4$ rods have a length of tens of micrometres and a diameter of the order of a few micrometres. For $CsAuX_4$ rods, the average crystallize size is calculated using Scherrer's formula given as:

$$D = {}^{k\lambda}\!/_{\beta_D cos\theta}$$

where D is the crystallite size, k is the shape factor (typically 0.94), λ is the wavelength of the X-ray used (1.5406 Å), β_D is broadening of the peak at half-maximal intensity (in radians) and θ is half of the diffraction angle. The average crystallite size decreases from 154.1 nm for $CsAuBr_4$ to 116.9 nm for $Cs_2Au_2Br_6$ as calculated using Scherrer's formula. Figure S3 shows the evolution of the morphology of $CsAuBr_4$ (Figure S3(a)-(c)) and $CsAuBr_3$ (Figure S3(d)-(f)) during external heat treatment. SEM images show the morphology of $CsAuBr_3$ changes from star-like to cube-shaped $Cs_2Au_2Br_6$ perovskite during the heat treatment. Figure 2 in the main manuscript corresponds to the SEM of 3 different samples prepared via wet chemical approach using the same set of precursors vis., CsCl and $AuCl_3$ in DI water which are then treated with different amounts of HBr to achieve the different phases. SEM images of $CsAuBr_4$ and $CsAuBr_3$ prepared using chemical method shows the rod-like and star-like (*truncated-cube*) morphology, respectively. However, when the amount of the HBr is increased in the solution, there is a change in the particle shape from star-like (*truncated-cube*) $CsAuBr_3$ to cube-shaped $Cs_2Au_2Br_6$. The formation of $Cs_2Au_2Br_6$ has also been achieved by a different process which requires heating of $CsAuBr_4$ and $CsAuBr_3$ at a higher temperature of around 220 °C for a complete transition. Figure S3(a) & (d) shows the SEM images of chemically synthesized $CsAuBr_4$ and $CsAuBr_3$ (annealed at 70 °C), respectively. Figure 3(c) & (f) shows the SEM images of $Cs_2Au_2Br_6$ prepared by annealing $CsAuBr_4$ and $CsAuBr_3$ at 220 °C, respectively. The direct comparison between Figure S3(c) & (f) and Figure 2(c) (for $Cs_2Au_2Br_6$) might not be accurate as the same phase of $Cs_2Au_2Br_6$ is obtained via two

completely different approaches since the shape and size of any material/compound depends greatly on the method of their preparation.[9, 10]

Moreover, we have tried to understand the shape evolution from $CsAuBr_4/CsAuBr_3 \rightarrow Cs_2Au_2Br_6$ during the heat treatment. $CsAuBr_3$ synthesized via chemical method is found to have star-like morphology (one kind of truncated cubic shape) which, after heat treatment, gets evolved into cube shaped $Cs_2Au_2Br_6$. On the other hand, $CsAuBr_4$ has rod-like shape and after annealing the compound, it preserves its shape though the phase evolves to $Cs_2Au_2Br_6$. As both the shapes (cube and rod; different aspect ratio) belongs to the same family, indirectly we can say that the morphology of $Cs_2Au_2Br_6$ obtained via two different methods are similar.

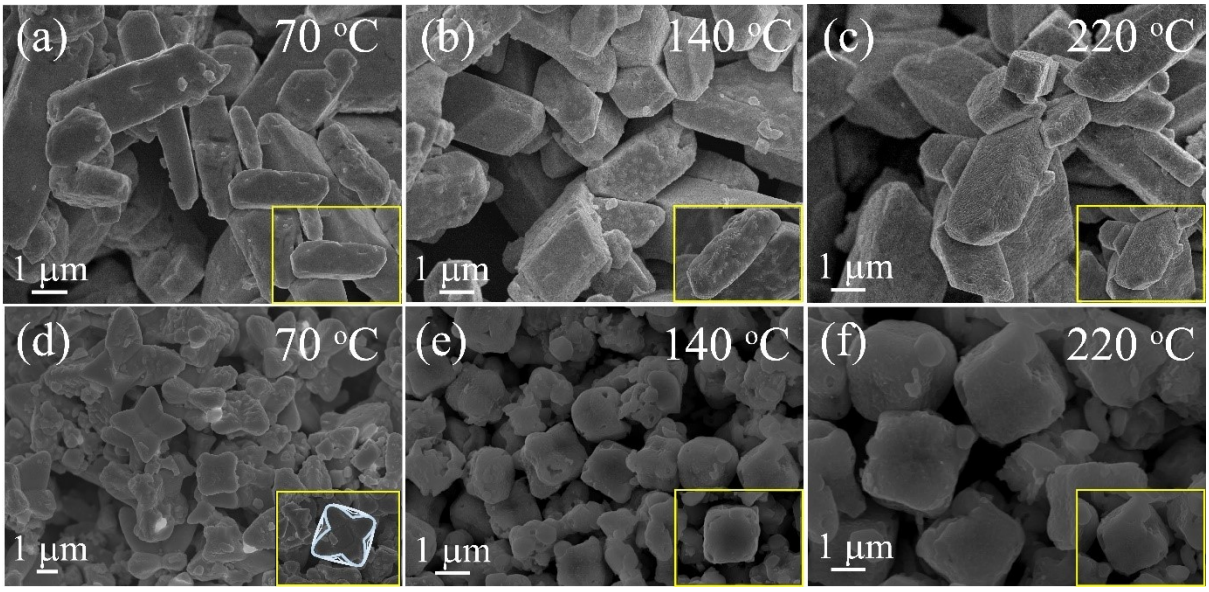

Figure S3: Evolution of the morphology of (a)-(c) $CsAuBr_4$ and (d)-(f) $CsAuBr_3$ with an increase in annealing temperature. SEM image shows that $CsAuBr_3$ has star-like morphology, which gradually transforms into cubic morphology marking the transition of cubic $CsAuBr_3$ to tetragonal $Cs_2Au_2Br_6$ at elevated temperatures.

The high-resolution photoelectron spectra as shown in Figure S4(a)-(c), reveal the core level spectra of C 1s, Cs 3d and Br 3d, respectively. The XPS spectra are corrected to the binding energy of 284.7 eV in accordance with the C 1s line of aliphatic (adventitious) carbon taken as reference. The two contributions $3d_{5/2}$ and $3d_{3/2}$, as observed for Cs 3d spectrum, located at 724.4 eV and 738.4 eV, correspond to Cs^+ cations and are in line with the literature data.[11] The Br 3d spectrum can be deconvoluted into two peaks at 68.5 eV and 69.9 eV corresponding to the binding energies of $3d_{5/2}$ and $3d_{3/2}$, respectively. The energy difference

between these deconvoluted peaks is ~1.4 eV and matches well with the previously reported results.[12]

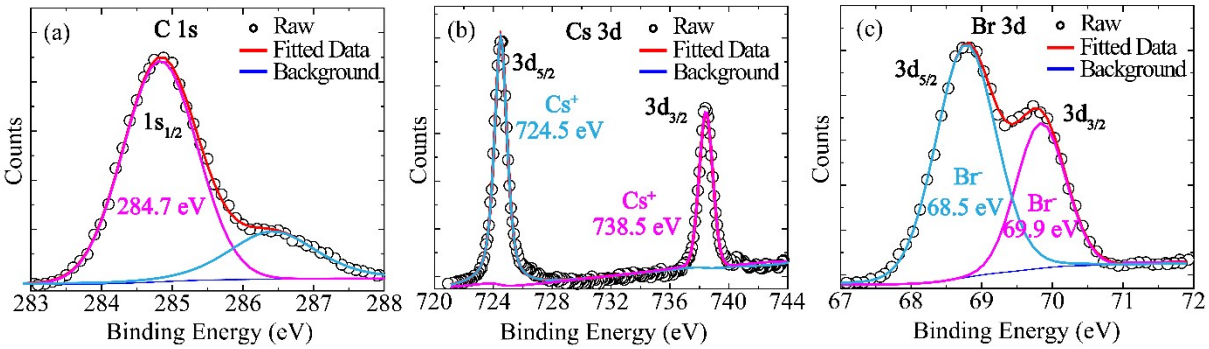

Figure S4: The high-resolution spectra for (a) C 1s, (b) Cs 3d and (c) Br 3d respectively. C 1s line of aliphatic carbon is used as a reference to correct the XPS spectra. The spectra corresponding to the core levels of Cs 3d and Br 3d indicate the presence of +1 and -1 oxidation states for Cs and Br, respectively.

In order to find the bandgap of as prepared powdered samples with x = 0, 25, 75, 100 and 200 µl of added HBr into the precursor solution of $CsAuCl_4$, UV-Vis spectroscopic measurement in the diffuse reflectance (DR) mode is performed over the spectral range of 400-1400 nm, and are shown in Figure S5. The DR spectrum, which is a plot between percentage reflectance and wavelength, is converted into pseudo-absorption data using the well-known Kubleka-Munk equation given by: $F(R_\infty) = \frac{K}{S} = \frac{(1-R_\infty)^2}{2R_\infty}$. Here, R_∞ is reflectance while K and S are the absorption and scattering coefficients of the sample, respectively.[13] The equation holds only when the scattering coefficient is independent of wavelength, which happens when the wavelength of the incident photons is less than the average grain size of the absorbing materials. The condition is satisfied for the bulk materials and thus, make Kubelka-Munk (K-M) function, $F(R_\infty)$, to match closely with the actual absorption spectra.[14]

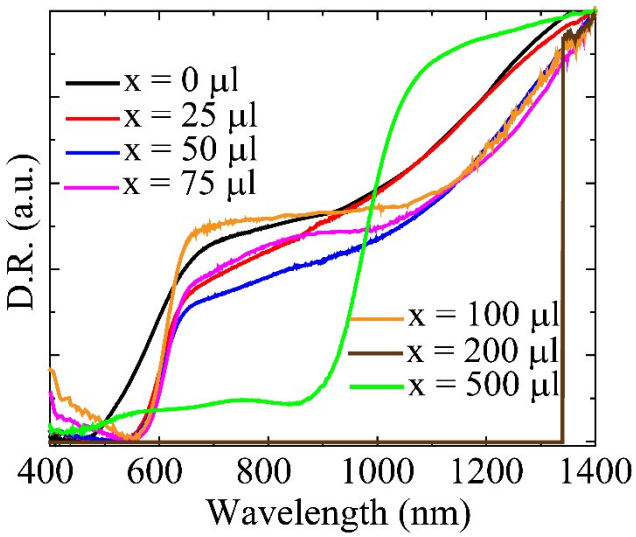

Figure S5: Diffuse reflectance (DR) spectra for $CsAuCl_4$ under treatment with different HBr concentrations (x =0, 25, 50, 75, 100, 200 and 500 µl).

The degree of disorder in $CsAuBr_4$ and $Cs_2Au_2Br_6$ is elucidated by making use of the sub-bandgap absorption edge of the absorption spectra, generally known as Urbach energy (E_u). E_u signifies density of deep defects, which act as recombination states in the bandgap of the material; a low value of which underlines the high tolerance to defects. The Urbach energy (E_u) is calculated using:

$$A \propto e^{E/E_u}$$

The rule is applicable within a section of the absorption spectrum which is explained by the "exponential distribution of the density of localized states in the tails of the allowed bands".[15] The exponential part near the optical band edge corresponds to Urbach tail. The sub-bandgap absorption mainly leads to this Urbach tail, which is observerd at lower energies (indicative of a disorderness in the system) and is followed by band-to-band transitions at higher energies. Therefore, for Urbach energy calculation, the fitting should be done only for exponential tails where, E < Eg (bandgap). Hence, we have fitted only that portion of the curve where, E < 1.98 eV for $CsAuBr_4$ and E < 1.4 eV for $Cs_2Au_2Br_6$. In our case, as shown in Figure S6, the value of E_u decreases from 347 meV to 75 meV as we change the Br concentration from 75 µl to 500 µl in $CsAuCl_4$, indicating the decrease in disorderness.

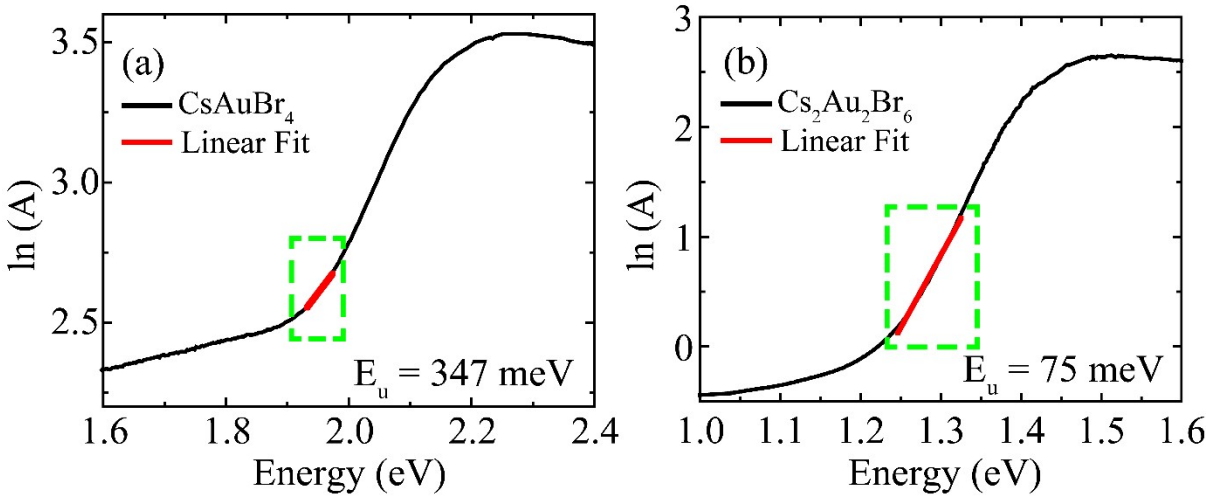

Figure S6: Experimentally calculated Urbach energies for (a) $CsAuBr_4$ (x = 75 µl HBr) and (b) $Cs_2Au_2Br_6$ (x = 500 µl HBr). Urbach energy is given by the inverse of the slope obtained from the graph ln(A) v/s energy.

Table S1: Direct and indirect bandgap values for $CsAuCl_4$ with a change in the quantity of HBr added.

Quantity of HBr, x (µl)	Direct Bandgap (eV)	Indirect Bandgap (eV)
0	2.32	1.96
25	2.10	1.94
50	2.07	1.95
75	1.98	1.89
100	1.96	1.80
200	-	-
500	1.41	1.38

Three phases of gold-based bromide perovskites were investigated theoretically to understand the stability, electronic structure, and the phase transition from one phase to another. The optimized structures of the three phases are shown in Figure S7.

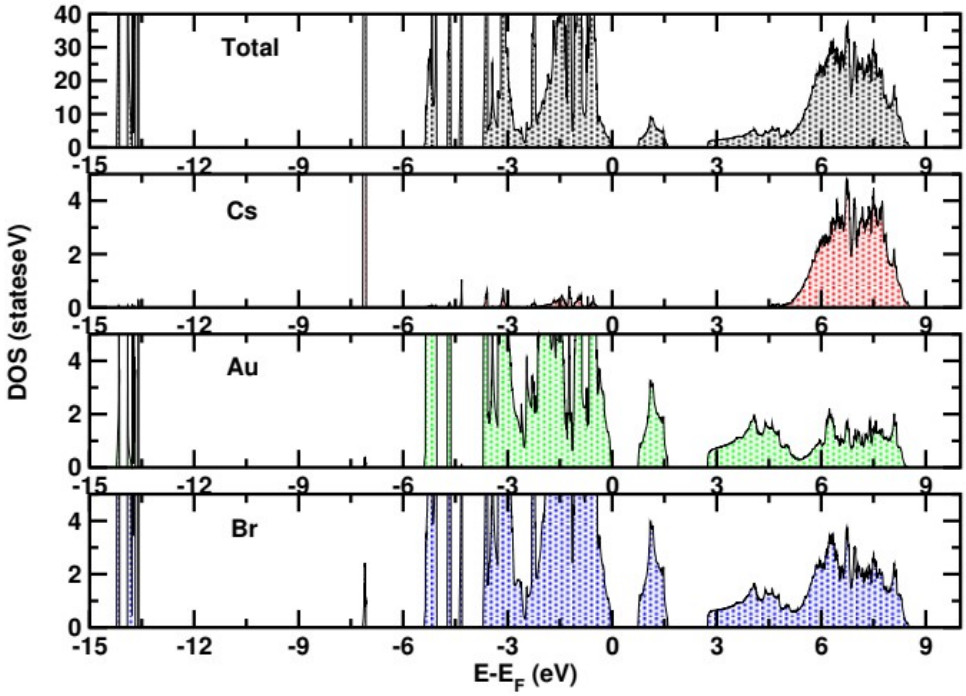

Figure S7: The total density of states for the monoclinic $CsAuBr_4$, along with the individual atomic contributions.

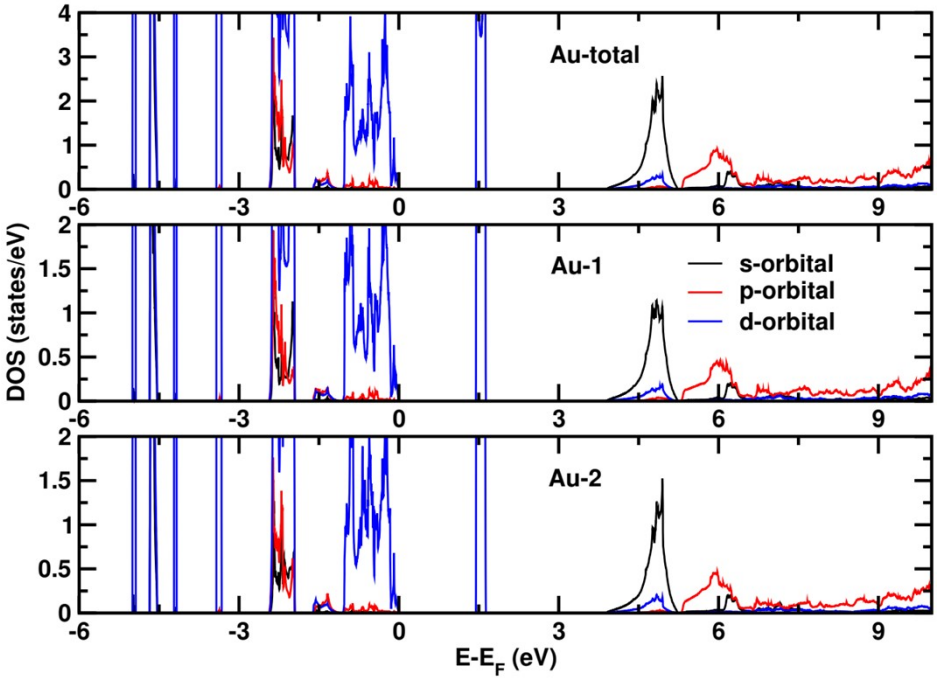

Figure S8: Density of states for the Au-atom of the monoclinic phase, $CsAuBr_4$ and the contributions from two different Au atoms (Au-1 and Au-2).

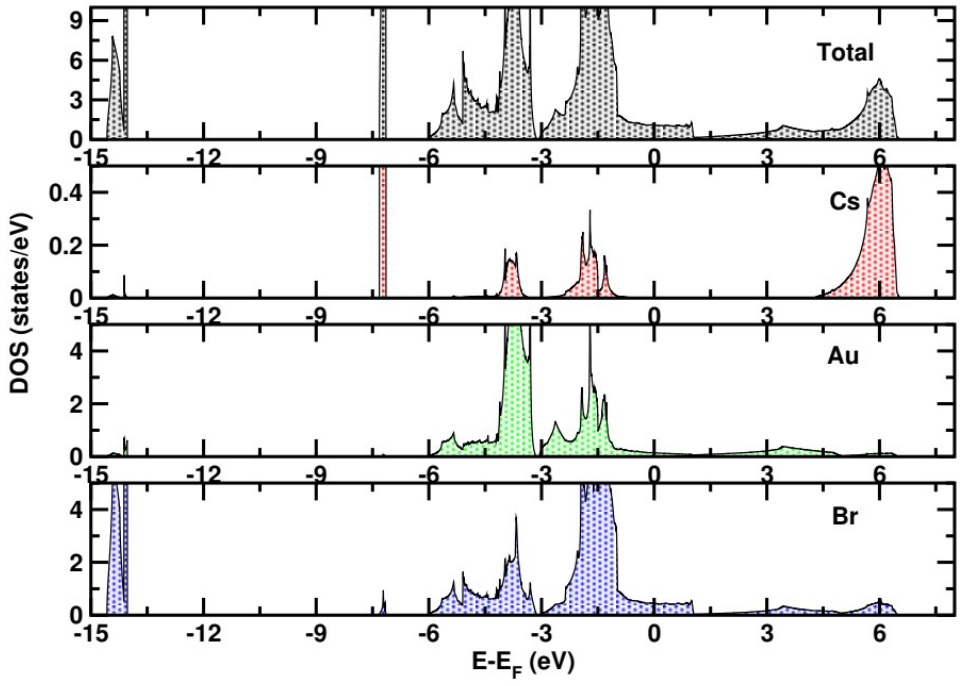

Figure S9: The total density of states for the cubic phase, $CsAuBr_3$, along with the individual atomic contributions.

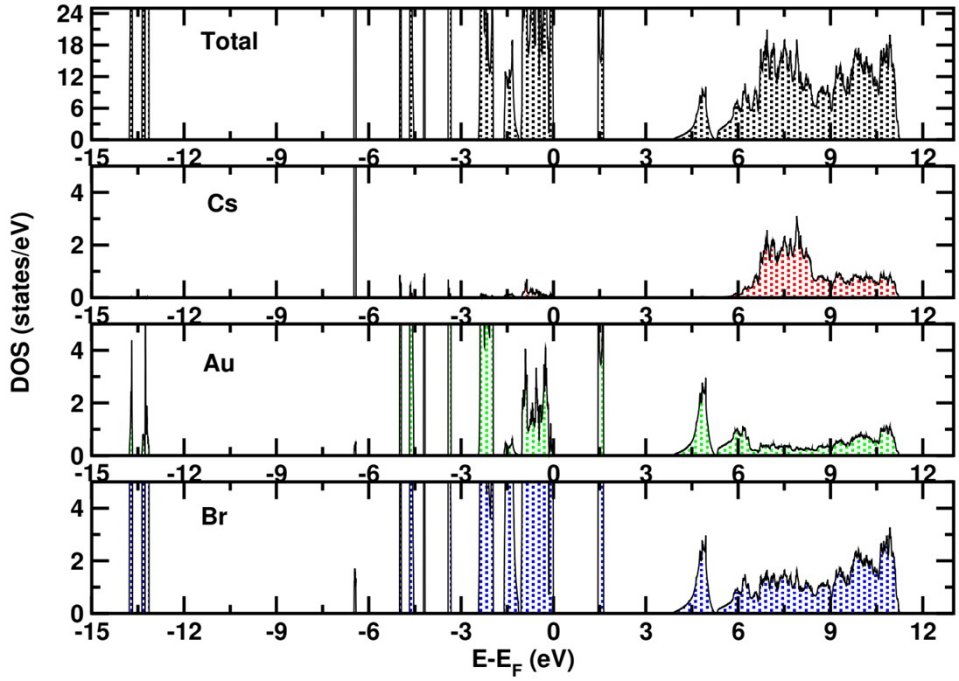

Figure S10: The total density of states for the tetragonal phase, $Cs_2Au_2Br_6$, along with the individual atomic contributions.

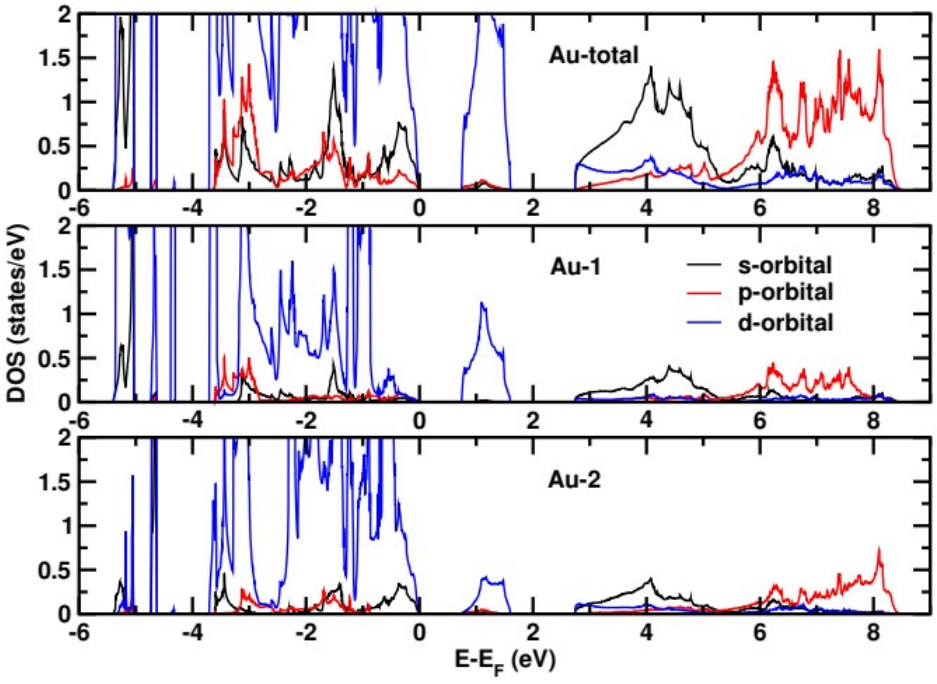

Figure S11: Density of states for the Au-atom of the tetragonal phase, $Cs_2Au_2Br_6$ and the contributions from two different Au atoms (Au-1 and Au-2).

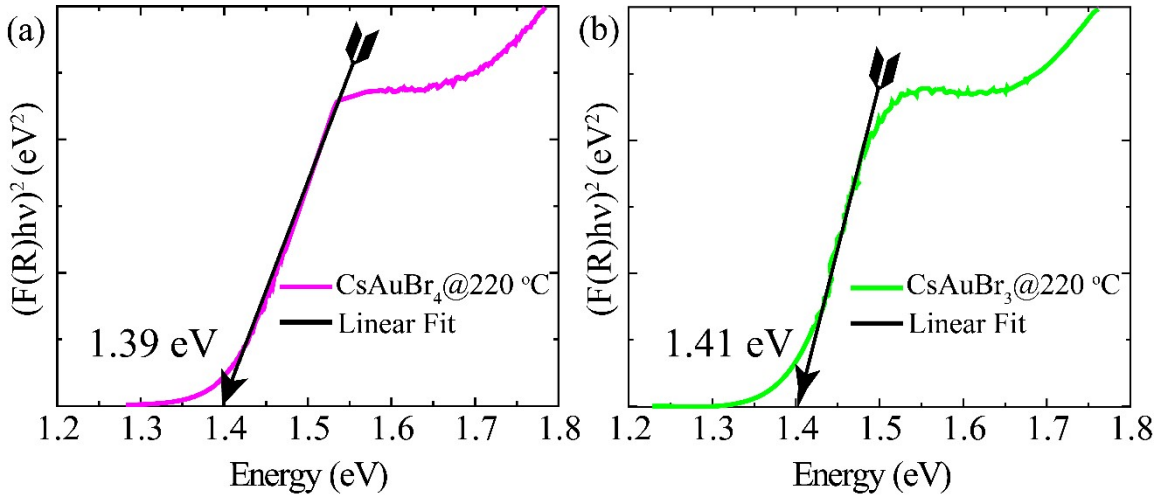

Figure S12: The direct bandgap obtained for $Cs_2Au_2Br_6$ via heating (a) $CsAuBr_4$ and (b) $CsAuBr_3$ at 220 °C.

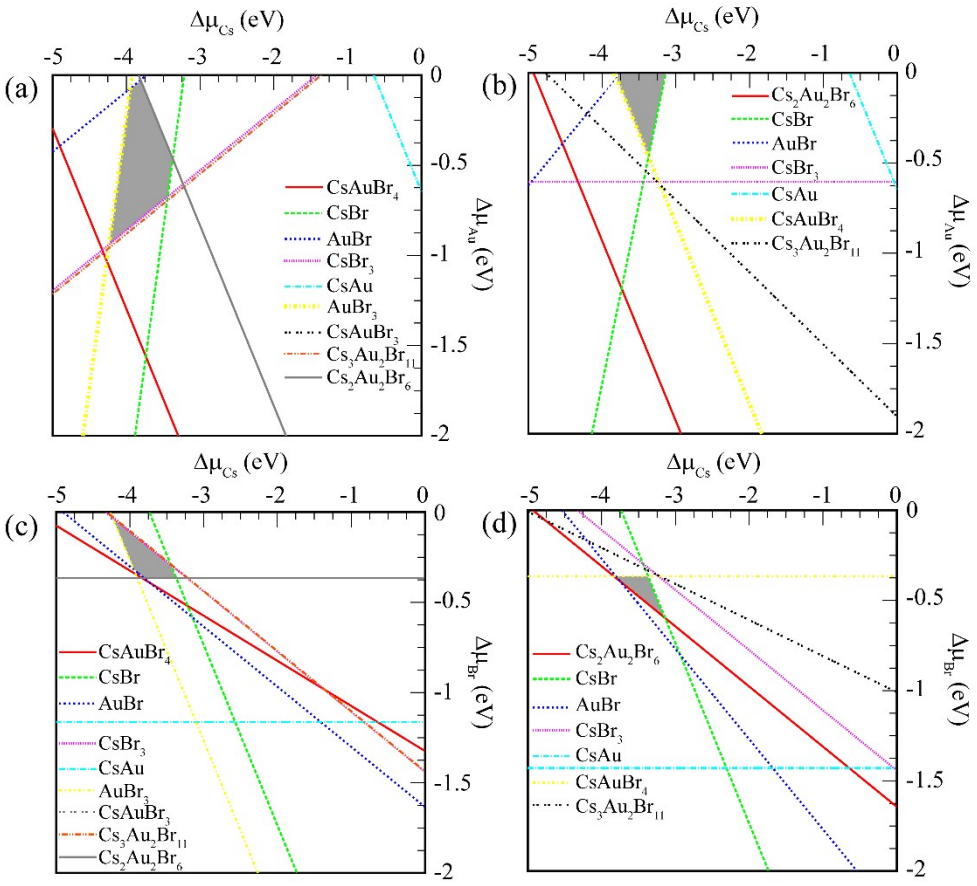

Figure S13: Simulated compositional phase diagram with respect to competing for secondary phases: (a) and (b) with respect to the change in chemical potential of Cs vs Au for $CsAuBr_4$ and $Cs_2Au_2Br_6$ phase respectively, and (c) and (d) with respect to the change in chemical potential of Cs vs Br for $CsAuBr_4$ and $Cs_2Au_2Br_6$ phase respectively. Grey shaded regions confirm the stability of the compounds and show the allowed chemical potential regions of constituent elements. Here, we are showing only the secondary phases which intersect the desired stability region.

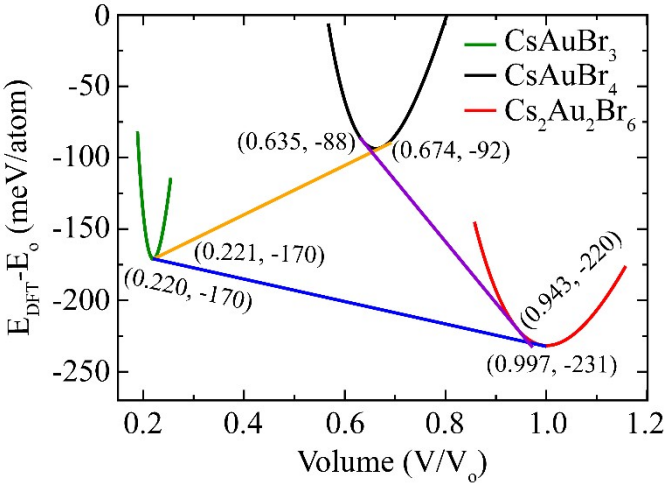

Figure S14: Comparison of the DFT ground state energy with the change in volume for the different phases. The blue line (common tangent) marks the points for the phase transition from cubic to tetragonal, orange line from cubic to monoclinic and purple line from monoclinic to tetragonal phase.

Table S2: Change in lattice parameters with temperature for $CsAuBr_3$.

Temperature (°C)	a (Å)	b (Å)	c (Å)
RT	5.52	5.51	5.50
50	5.54	5.50	5.50
100	5.55	5.42	5.50
150	5.56	5.50	5.59
180	7.86	7.90	11.48
200	7.88	7.90	11.48
220	7.88	7.90	11.48

References:

1. Hohenberg, P.; Kohn, W., Inhomogeneous Electron Gas. *Physical Review* **1964,** *136* (3B), B864-B871.
2. Kresse, G.; Furthmüller, J., Efficient iterative schemes for ab initio total-energy calculations using a plane-wave basis set. *Physical Review B* **1996,** *54* (16), 11169-11186.
3. Kresse, G.; Furthmüller, J., Efficiency of ab-initio total energy calculations for metals and semiconductors using a plane-wave basis set. *Computational Materials Science* **1996,** *6* (1), 15-50.
4. Kresse, G.; Hafner, J., Ab initio molecular dynamics for liquid metals. *Physical Review B* **1993,** *47* (1), 558-561.
5. Blöchl, P. E., Projector augmented-wave method. *Physical Review B* **1994,** *50* (24), 17953-17979.
6. Perdew, J. P.; Burke, K.; Ernzerhof, M., Generalized Gradient Approximation Made Simple. *Physical review letters* **1996,** *77* (18), 3865-3868.
7. Blöchl, P. E.; Jepsen, O.; Andersen, O. K., Improved tetrahedron method for Brillouin-zone integrations. *Physical Review B* **1994,** *49* (23), 16223-16233.
8. Li, T.; Mo, X.; Peng, C.; Lu, Q.; Qi, C.; Tao, X.; Ouyang, Y.; Zhou, Y., Distinct green electroluminescence from lead-free CsCuBr2 halide micro-crosses. *Chemical Communications* **2019,** *55* (31), 4554-4557.
9. Wu, Z.; Yang, S.; Wu, W., Shape control of inorganic nanoparticles from solution. *Nanoscale* **2016,** *8* (3), 1237-1259.
10. Dong, B.-X.; Qiu, F.; Li, Q.; Shu, S.-L.; Yang, H.-Y.; Jiang, Q.-C., The Synthesis, Structure, Morphology Characterizations and Evolution Mechanisms of Nanosized Titanium Carbides and Their Further Applications. *Nanomaterials* **2019,** *9* (8).
11. Zhang, C.; Gao, L.; Teo, S.; Guo, Z.; Xu, Z.; Zhao, S.; Ma, T., Design of a novel and highly stable lead-free Cs_2NaBiI_6 double perovskite for photovoltaic application. *Sustainable Energy & Fuels* **2018,** *2* (11), 2419-2428.
12. Cai, Y.; Wang, L.; Zhou, T.; Zheng, P.; Li, Y.; Xie, R.-J., Improved stability of CsPbBr3 perovskite quantum dots achieved by suppressing interligand proton transfer and applying a polystyrene coating. *Nanoscale* **2018,** *10* (45), 21441-21450.
13. Morales, A. E.; Mora, E. S., Use of diffuse reflectance spectroscopy for optical characterization of un-supported nanostructures. *Revista Mexicana De Fisica* **2007,** *53* (5), 18-22.
14. Kortüm, G., Reflectance Spectroscopy: Principles, Methods, Applications. *Springer Science & Business Media* **2012**.

15. Zaynobidinov, S.; Ikramov, R. G.; Jalalov, R. M., Urbach energy and the tails of the density of states in amorphous semiconductors. *Journal of Applied Spectroscopy* **2011,** *78* (2), 223-227.